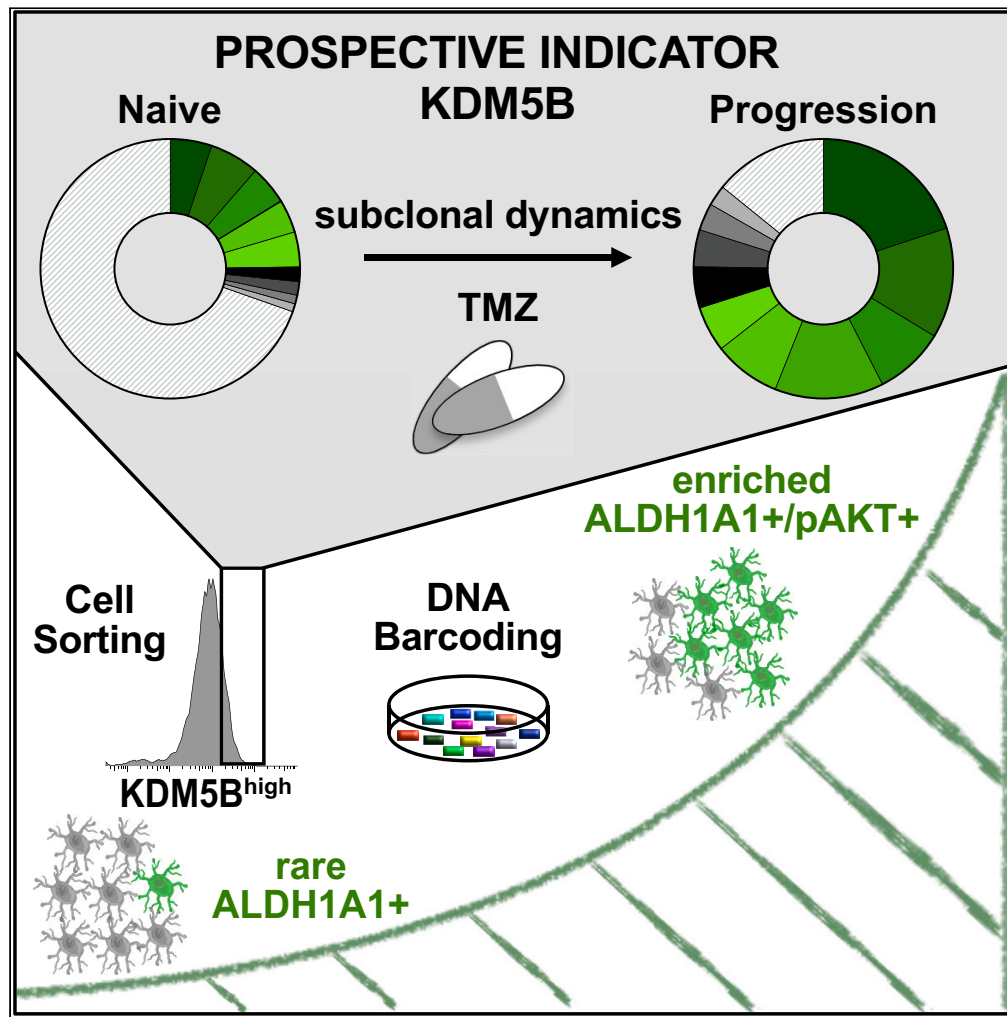# iScience

Article

KDM5B predicts temozolomide-resistant subclones in glioblastoma

Vivien Ullrich,
Sarah Ertmer,
Anna Baginska, ...,
Alexander Roesch,
Barbara M. Grüner,
Björn Scheffler

vivien.ullrich@uk-essen.de

Highlights

Temozolomide triggers KDM5B-expressing naive glioblastoma cells

KDM5B dynamics occurs in the hierarchy of a rare ALDH1A1+ subpopulation

Resilient KDM5B^{high} cells mediate AKT-driven progression under temozolomide

Barcoding suggests predictive value of KDM5B^{high} cells for subclonal expansion

iScience

Article

KDM5B predicts temozolomide-resistant subclones in glioblastoma

Vivien Ullrich,[1,2,3,4,*] Sarah Ertmer,[1,2,3,4] Anna Baginska,[1,2,3,5] Madeleine Dorsch,[2,3,5] Hanah H. Gull,[1,3,6,7] Igor Cima,[1,2,3,4] Pia Berger,[1,2,3,4] Celia Dobersalske,[1,2,3,4] Sarah Langer,[1,2,3,4] Loona Meyer,[1,2,3,4] Philip Dujardin,[2,3,5] Sied Kebir,[1,2,3,7,8] Martin Glas,[1,2,3,7,8] Tobias Blau,[9] Kathy Keyvani,[9] Laurèl Rauschenbach,[1,2,3,6,7] Ulrich Sure,[2,3,6,7] Alexander Roesch,[2,3,10,11] Barbara M. Grüner,[2,3,5,11,12,13] and Björn Scheffler[1,2,3,4,11,12,13,14]

SUMMARY

Adaptive plasticity to the standard chemotherapeutic temozolomide (TMZ) leads to glioblastoma progression. Here, we examine early stages of this process in patient-derived cellular models, exposing the human lysine-specific demethylase 5B (KDM5B) as a prospective indicator for subclonal expansion. By integration of a reporter, we show its preferential activity in rare, stem-like ALDH1A1+ cells, immediately increasing expression upon TMZ exposure. Naive, genetically unmodified KDM5B^{high} cells phosphorylate AKT (pAKT) and act as slow-cycling persisters under TMZ. Knockdown of _KDM5B_ reverses pAKT levels, simultaneously increasing PTEN expression and TMZ sensitivity. Pharmacological inhibition of PTEN rescues the effect. Interference with _KDM5B_ subsequent to TMZ decreases cellular vitality, and clonal tracing with DNA barcoding demonstrates high individual levels of KDM5B to predict subclonal expansion already before TMZ exposure. Thus, KDM5B^{high} treatment-naive cells preferentially contribute to the dynamics of drug resistance under TMZ. These findings may serve as a cornerstone for future biomarker-assisted clinical trials.

INTRODUCTION

Many models of the origin, development, and persistence of cancer are based on circumscribed populations of cells. Pre-existing cancer stem cells or any group of highly plastic and adaptive cells may contribute to the population dynamics observed under the effect of clinical treatment in glioblastoma, the most malignant brain tumor of adulthood.[1–4] We have recently described a rare ALDH1A1+, stem-like cell population in treatment-naive glioblastoma that acquires pAKT and subclonally expands under the influence of TMZ in models of disease and during clinical progression.[5] We were curious to follow up on the observation, aiming to decipher the early mechanisms that promote this cellular behavior. It is considered that adaptive plasticity of glioblastoma cells may be the result of a cooperation and interplay of genetic events and epigenetic adaptions that jointly lead to drug resistance.[6] Notably, data acquired from large, paired patient cohorts obtained before and after therapy indicated overall comparable genetic patterns without evidence of profound treatment-specific alterations. Rather, these data suggest that cellular dynamics, under the pressure of treatment, descends from pre-existing rare cell populations at primary disease.[7,8] Research in melanoma, lung, and breast cancer has established phenotypic cell state transitions and drug tolerance on an epigenetic level, e.g., by investigating KDM5A+ or KDM5B+ drug-tolerant persister cells.[9–12] In glioma/glioblastoma, KDM5A or KDM5B have been suggested to mediate the acquisition of TMZ resistance[13–17] and pre-existing slow-cycling cells characterized by KDM6A/B expression and Notch signaling were described to prevail under the treatment of receptor tyrosine kinase inhibitors.[18] In this study, we hypothesized that KDM

[1]DKFZ-Division Translational Neurooncology at the WTZ, DKTK partner site, University Hospital Essen, 45147 Essen, Germany
[2]German Cancer Consortium (DKTK), partner site Essen/Düsseldorf, a partnership between DKFZ and University Hospital Essen, Germany
[3]West German Cancer Center (WTZ), University Hospital Essen, 45147 Essen, Germany
[4]German Cancer Research Center (DKFZ), 69120 Heidelberg, Germany
[5]Department of Medical Oncology, West German Cancer Center, University Hospital Essen, University Duisburg-Essen, 45147 Essen, Germany
[6]Department of Neurosurgery and Spine Surgery, University Hospital Essen, 45147 Essen, Germany
[7]Center for Translational Neuroscience and Behavioral Science (C-TNBS), University of Duisburg-Essen, 45147 Essen, Germany
[8]Division of Clinical Neurooncology, Department of Neurology, University Hospital Essen, 45147 Essen, Germany
[9]Department of Neuropathology, University Hospital Essen, 45147 Essen, Germany
[10]Department of Dermatology, University Hospital Essen, 45147 Essen, Germany
[11]Center of Medical Biotechnology (ZMB), University Duisburg-Essen, 45141 Essen, Germany
[12]Senior author
[13]These authors contributed equally
[14]Lead contact
*Correspondence: vivien.ullrich@uk-essen.de
https://doi.org/10.1016/j.isci.2023.108596

family genes were involved in adaptive plasticity, that is, the early response of selected tumor cells to first-time TMZ-exposure leading to drug resistance and subsequent subclonal enrichment.

RESULTS

Presence and dynamics of KDM5B^{high} cells under TMZ exposure

As an entry route to the investigation of TMZ-resistant cell states, we screened the described KDM family genes for their potential involvement in the TMZ-driven expansion of ALDH1A1+ cellular hierarchies (Figure 1A). We used an established cohort[5] of short-term *in vitro* expanded, vital patient cells representing pairs of treatment-naive and respective TMZ-experienced relapse samples derived from n = 8 *IDH*-wt glioblastoma individuals (Table S1). Quantitative assessment via qPCR did not reveal a correlation of *ALDH1A1* expression levels between the pairs of treatment-naive vs. relapse samples (Figures 1B and S1A). Thus, an enrichment of ALDH1A1+ relapse cells could not be predicted from the original *ALDH1A1* expression in the treatment-naive samples. In contrast, *KDM5B* expression in naive samples, but not *KDM5A* nor *KDM6A*, significantly correlated with the enrichment of *ALDH1A1* expression in the paired relapse cell samples (Figures 1C–1E and S1B). In this line, experimental short-term exposure of TMZ to naive cells led to a robust increase of ALDH1A1/KDM5B-coexpression *in vitro* (Figures 1F and S1C). Interestingly, this increase could not be recapitulated by exposure of the drug dasatinib, which has been described to induce KDM6-mediated adaptive chromatin remodeling and drug tolerance in glioblastoma models.[18] Similarly, the drug lomustine that is clinically relevant for glioblastoma treatment in combinatorial settings[19,20] did not induce an increase of coexpression. This suggested a TMZ-specific effect on KDM5B-expressing ALDH1A1+ cells.

KDM5B is a H3K4 demethylase, traditionally considered as a biomarker for slow-cycling drug tolerant persister cells, e.g., in melanoma or breast cancer.[21,22] We therefore stably integrated an EGFP-based reporter construct[9] to visualize the dynamics of *KDM5B* expression in the primary cell models (n = 6 from 4 patients, see STAR Methods) (Figures 1G and S1D). In an index case, we studied the prolonged effect of a 16-day TMZ exposure (TMZ-on), followed by withdrawal of the drug and continuous maintenance of the cells *in vitro* (TMZ-off). The TMZ-on stage of the experiment resulted in a >90% reduction of cell confluence. During the TMZ-off stage of the experiment, we observed a period of 3–4 weeks of quiescence before clonal expansion occurred (long-term assay from[5]). For comparative evaluation along the initial course of this assay, we determined the fluorescence intensity of the naive top 5% EGFP-KDM5B+ cells as a reference (KDM5B^{high}). The relative number of KDM5B^{high} cells that reached this threshold was then scored for all subsequent experimental populations in the test. We observed that the number of KDM5B^{high} cells doubled during TMZ-on, and that it peaked with an increase of 800% during TMZ-off at one week after TMZ withdrawal, to constantly decrease thereafter. By contrast, expression levels of the reporter construct remained stable in naive cells during the observation period (Figures 1H and S1D). Furthermore, increasing expression levels of *KDM5B* could be recorded from the bulk of naive tumor cells upon drug exposure, using n = 5 genetically unmodified clinical glioblastoma cell samples. At the peak of TMZ-off (i.e., on day 23 of the long-term assay), *KDM5B* expression transiently increased by a factor of 2.86 compared to the original treatment-naive stage (Figure S1E).

Moreover, early TMZ effects could be observed using reductionist *in vitro* drug exposure schedules involving condensed periods of TMZ-on for 2–5 days, followed by 3–8 days TMZ-off before experimental readout. The frequency of KDM5B^{high} cells in these assays increased significantly, by a factor of 2.3 in TMZ pre-exposed clinical and experimental relapse samples, and even more pronounced, by a factor of 3.2 in treatment-naive patient cells (Figures 1I and S1F). Increasing levels of KDM5B were observed in reporter-based assays and confirmed in genetically unmodified naive patient cells (Figures S1G and S1H).

7-AAD-based flow cytometry assays indicated that significantly more viable KDM5B^{high} cells were present at this stage than viable KDM5B^{low} cells ([KDM5B−EGFP]naive patient samples; Figure 1J). CellTrace experiments additionally revealed that KDM5B^{high} cells were slow-cycling, because their high EGFP-reporter fluorescence intensity overlapped with the most intense peaks of CellTrace dye at the end of the assay (Figure 1K).

Thus, experimental evidence indicated that the early effects of TMZ exposure involved high endogenous expression levels of KDM5B in a rare subpopulation of slow-cycling cells. The overlap with cellular ALDH1A1 furthermore indicated an involvement in the process of TMZ-triggered acquisition of AKT-mediated drug resistance during subclonal progression in glioblastoma.

KDM5B mediates cellular TMZ response through the PTEN-AKT axis

To reveal an immediate relationship of TMZ-triggered KDM5B expression and phosphorylated AKT, we subsequently focused solely on the study of genetically unmodified, treatment-naive cell samples in the condensed drug exposure assays. Other groups already reported on the interaction of KDM5B with the PI3K-AKT signaling, e.g., via direct binding of the promoter region and consequent suppression of PTEN,[23] or PIK3CA.[24]

In flow cytometry-based assays, we observed that short-term TMZ exposure led to a significant increase of pAKT (Ser473) in the overall cell population, by a factor of 1.6 on day 5 (Figures 2A and S2A). The frequency of KDM5B+/pAKT+ cells simultaneously increased by a factor of 3.2. These effects were not observed under exposure of the alternative therapeutics dasatinib or lomustine (Figures 2B and S2B) and we could confirm that high KDM5B protein levels occurred in the hierarchy of ALDH1A1+/pAKT+ cells (Figures 2C and S2C). Notably, the knockdown of *KDM5B* did not affect PI3K, but resulted in a rapid inhibition of AKT activity in the treatment-naive cells (Figures 2D and S2D–S2H), while the expression of its negative regulator PTEN increased (Figures 2D, 2E, S2E, S2G, and S2H). Consequently, sequential exposure of TMZ and siRNA-mediated *KDM5B* knockdown had an additive-negative effect on cellular viability, which could be rescued by post-hoc supply of SF1670, a potent and specific small molecule inhibitor of PTEN[25] (Figures 2F, S2E, S2G, and S2H). We then speculated that KDM5B could directly suppress *PTEN* expression by interfering with accessibility to its promoter via Histone 3 demethylation at lysine 4 (H3K4). However,
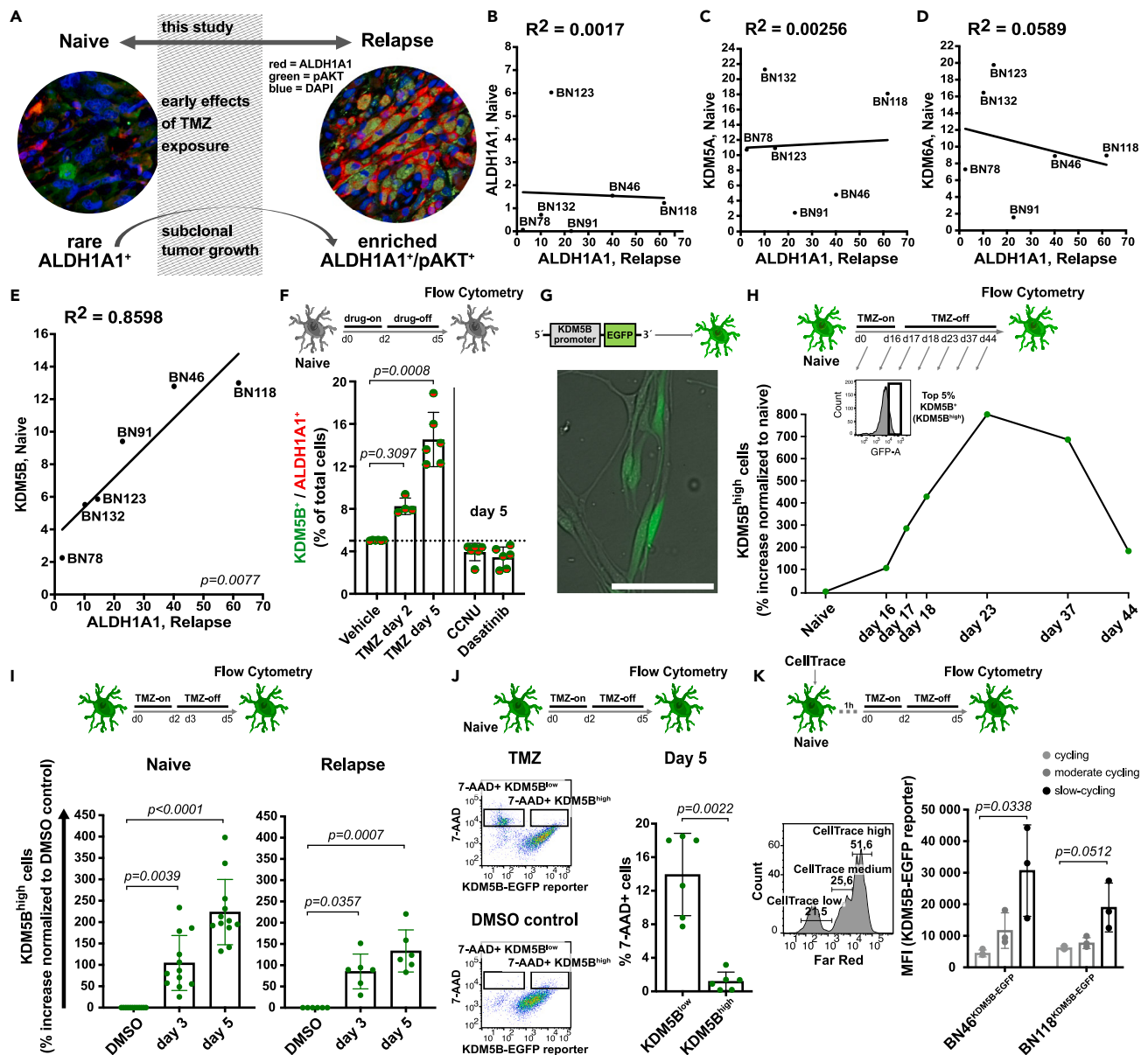
Figure 1. Presence and dynamics of KDM5B^{high} cells under TMZ exposure

(A) Cartoon illustrating the rationale of this study. Visualized is the TMZ-mediated enrichment of subclones observed at disease relapse. Representative immunofluorescent appearance of cellular phenotypes in patient tissue at primary disease (Naive) and after clinical treatment (Relapse).[5]

(B–E) Graphs depict personalized qPCR-based gene expression values of short-term expanded pairs of patient cell samples. Patient IDs indicated. Mean of triplicate. R^2, Pearson coefficient of determination. Treatment-naive expression levels of *ALDH1A1* (B), *KDM5A* (C), *KDM6A* (D), and *KDM5B* (E) were correlated with the *ALDH1A1* levels of respective relapse samples.

(F) Bar chart showing frequency of co-expressing cells at the indicated time points of the treatment scheme: drug-on, exposure to vehicle (0.5% DMSO or 0.1% ethanol), or 500 μM TMZ, or 50 μM CCNU, or 10 μM dasatinib; drug-off, no drug exposure. Flow cytometry analysis, in duplicate/triplicate on sample IDs BN46, BN118; presented as mean ± SD. p values obtained by Kruskal-Wallis with Dunn's post-hoc test.

(G) Phase contrast appearance and vital EGFP fluorescence of representative patient cell sample (naive-E049) transduced with KDM5B promoter-EGFP reporter construct as indicated by the cartoon (pLU-JARID1Bprom-EGFP-BLAST, provided by a study by Roesch et al.).[9] Scale bar, 100 μM.

(H) Graph plotting flow cytometry data obtained from KDM5B^{high} subpopulations of reporter construct-transduced, naive BN46$^{KDM5B-EGFP}$ patient cells. Time points and TMZ (500 μM) -on/-off schedule as indicated. Data represent the percent increase of KDM5B^{high} cells (relative number of cells that reached the set fluorescence threshold), normalized to the naive time point.

(I) Bar plots depicting the increase of KDM5B^{high} subpopulations in reporter construct-bearing naive (BN46$^{KDM5B-EGFP}$, BN118$^{KDM5B-EGFP}$, E049$^{KDM5B-EGFP}$, E056$^{KDM5B-EGFP}$) and relapse ($^{TMZ\rightarrow eR}$BN46 $^{KDM5B-EGFP}$, ^{cR}BN118 $^{KDM5B-EGFP}$) patient cell samples (compare Table S1). Time points and TMZ (500 μM)

Figure 1. Continued

-on/-off schedule as indicated. Values normalized to corresponding (0.5%) DMSO controls and shown as mean ± SD. p values calculated using a Kruskal-Wallis test with Dunn's post-hoc test.

(J) Bar plot indicating 7-AAD+ cell frequencies in KDM5B^{high} vs. KDM5B^{low} subpopulations of construct-bearing naive BN46[KDM5B−EGFP] and naive BN118[KDM5B−EGFP] patient cell samples. Triplicate data, obtained by flow cytometry after TMZ (500 μM) -on/-off schedule as indicated, shown as mean ± SD. Left inset: Representative plots (BN46[KDM5B−EGFP]), including (0.5%) DMSO-control. p value by Wilcoxon rank-sum test (gated).

(K) CellTrace experiment. Histogram of *Far Red* peaks revealing high, moderate, and slow-cycling subpopulations by flow cytometry (representative case, naive BN118[KDM5B−EGFP]). Bar chart representing mean fluorescence intensity (MFI) of KDM5B-EGFP reporter for each *Far Red* peak. Triplicate data as mean ± SD. p values by Kruskal-Wallis test.

See also Figure S1 and Table S1.

we could not verify this hypothesis in CHIP-seq experiments by use of a polyclonal H3K4trimethylation antibody. Other players of the PI3-Kinase pathway, i.e., PIK3CA, AKT 1/2/3, and mTOR, appeared similarly unaffected (Figure S2I), indicating either the need for a more selective analysis of the rare KDM5B^{high} cells, or that the effects of KDM5B may not be caused by its histone demethylase activity at the respective promoter regions. To nevertheless validate that KDM5B inhibition causes increased TMZ sensitivity, we applied molecular and pharmacological interference assays. siRNA-mediated knockdown of *KDM5B* or application of CPI-455, a pan-KDM5 inhibitor,[26] subsequent to TMZ exposure, indeed resulted in marked increases of active caspase-3 compared to the TMZ-only schedule (Figures 2G and 2H). Within 12 days, the cellular viability of naive patient cells decreased significantly stronger under the combinatorial sequence of TMZ→CPI-455 compared to the TMZ-only schedule, resulting in a viability reduction of 80 ± 2% vs. 52 ± 5%, respectively. Similar effects on cellular viability were elicited by C46, an alternative inhibitor of KDM5B[27] (Figure 2I).

These data indicate that KDM5B acts as an early mediator of cellular response to TMZ, by modulating the PTEN-AKT axis preferentially in the hierarchy of rare ALDH1A1+ cells to enable subsequent acquisition of drug resistance. It is tempting to speculate that the endogenous expression levels of KDM5B are decisive for the empowering of individual treatment-naive cells to adapt quickly to TMZ exposure. In fact, one would expect TMZ-triggered KDM5B^{high} naive cells to kick-off generations of daughter cells that would expand to a subclonal hierarchy under therapeutic pressure.

KDM5B expression predicts TMZ-triggered subclonal growth

To experimentally address the hypothesis that particular cellular identities are responsible for subclonal expansion, we employed cellular barcoding technology for "unsupervised" mapping of population dynamics in response to TMZ. We considered cellular heterogeneity in the original, treatment-naive patient samples at the time of barcoding. We anticipated next to a static bystander pool of cells, both, dominant and newly arising/originally underrepresented, cellular hierarchies to become responsible for the shifting of the subclonal composition along the course of primary treatment (Figure 3A).

We studied two treatment-naive, patient-specific cell samples applying the following experimental schedule (BN46, BN118; compare Figure 1H): one million individual patient cells were DNA-barcoded with a Clontracer construct[28] via lentiviral transduction (*Prepool*) and expanded for three passages to generate n = 8 *in vitro* replicates (*Naive*). These cells were then exposed to DMSO as a control ([DMSO]CTRL) or treated with TMZ for 16 days, according to our established assay.[5] After TMZ exposure, ~10% TMZ-resistant cells (TMZ-r) survived, and 2–4 weeks later, cellular progression occurred by expanding TMZ-resistant cells (TMZ-rex) (Figure 3B). Representative cellular samples were derived from each of these steps and processed for next-generation sequencing (NGS).

Bioinformatic pipeline analysis revealed the frequency of barcode identities (BCIs) from the respective bulk of tumor cells. Considering both patients, we observed the detectable BCIs to drop below 0.3% during the *in vitro* expansion phase that generated the replicates for the experiment (Prepool-BCIs = 10[6] ± 11,313 vs. *Naive*-BCIs = 2,900 ± 3,343) (Figure 3C). It is important to note that BCIs were detected with respect to a threshold set by the bioinformatic pipeline. Rare reads can in this analysis be classified as "undetectable," even though the cellular identities are present in the overall population of investigated cells. An expansion of multiple subclones with dissimilar growth kinetics will always increase the prevalence of dominant subclones (i.e., identified BCIs) in the population and simultaneously decrease the prevalence of others so much that they can fall under the detection threshold (i.e., undetectable BCIs).[28,29] As a consequence, the frequency of identified BCIs decreases and the frequency of undetectable BCIs increases over time, unless dominant subclones are reduced by therapeutic intervention. Consequently, the 16-day TMZ exposure in our assay led to a remarkable re-emergence of >250,000 TMZ-r-BCIs (259,886 ± 346,177), which declined again in the progressing TMZ-rex (BCIs = 6,613 ± 5,964) (Figure 3C). This suggested the presence of dominant subclones, but surprisingly, we also detected newly arising BCIs that were most abundant among TMZ-rex (70% in BN118 and 55% in BN46; Figures 3D, 3E, S3A, and S3B). Their enrichment occurred secondary to a loss of drug-sensitive dominant subclones and as a consequence of the "uncovering" of thousands of underrepresented BCIs in the TMZ-r. Among these new candidate subclones, however, only very few continued to thrive to become "newly arising" TMZ-rex hierarchies of tumor cells. At that stage, they nevertheless collectively outnumbered the originally dominant BCIs and they accumulated in the top 10 ranked list of TMZ-rex BCIs (Figures 3F and S3C).

Intriguingly, we could demonstrate strongly increased *ALDH1A1* mRNA levels among the TMZ-rex populations (Figure S3D), but as an inherent drawback of DNA barcoding, we could not directly relate this to the early effects of dynamic *KDM5B* levels in individual cells. We therefore decided to sort-out KDM5B^{high} cellular identities from the barcoded heterogeneous samples at the *Naive* stage to determine the BCI composition and to subsequently follow their course by comparative investigation with the bulk of barcoded tumor cells (Figures 3G and S3E). Remarkably, we observed in every replicate analysis the top-ranked BCIs of the sorted KDM5B^{high} cell sample to almost
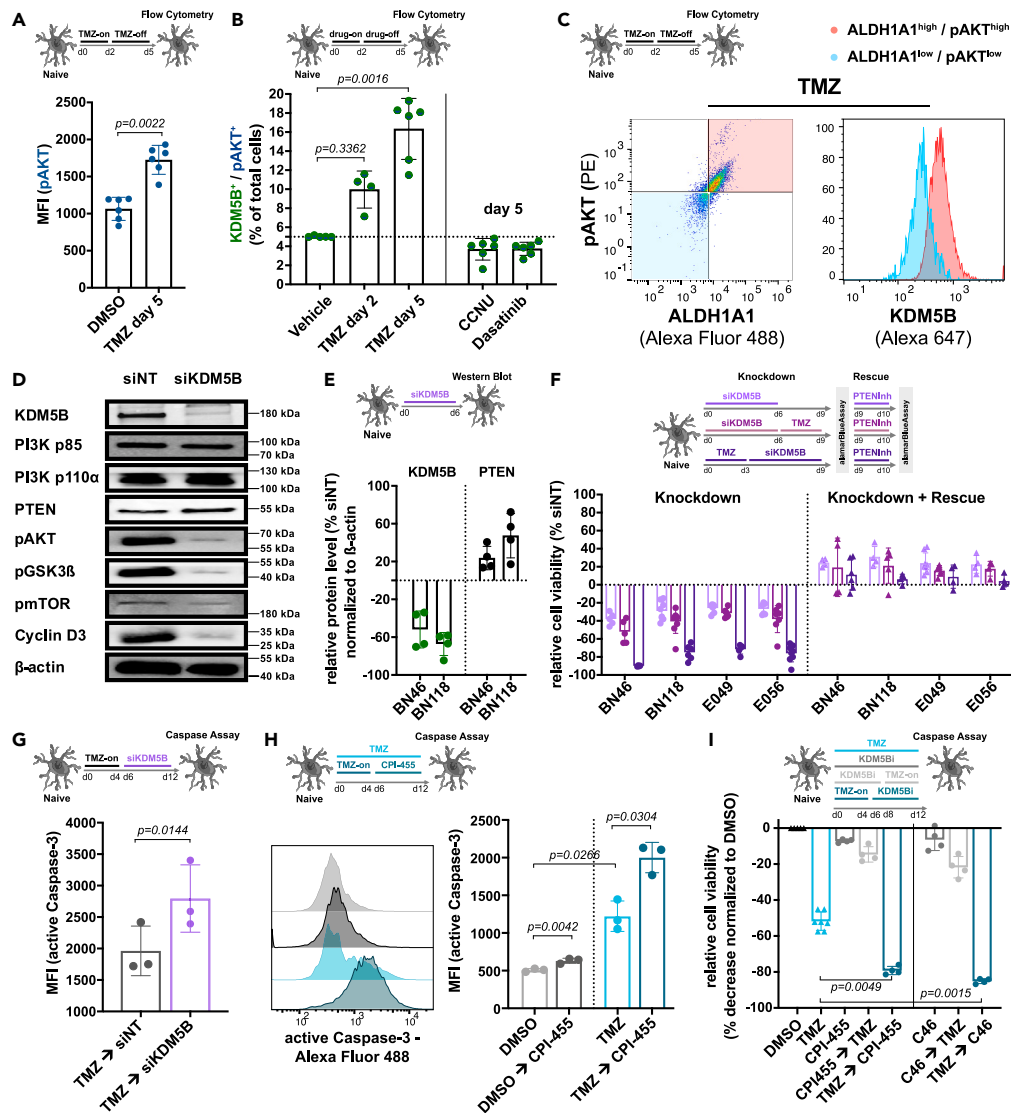
Figure 2. KDM5B mediates cellular TMZ response through the PTEN-AKT axis

(A) Bar chart depicting flow cytometry MFI data obtained from two naive patient samples (BN46, BN118). Treatment scheme as indicated, comprised TMZ (500 μM) -on/-off periods vs. 0.5% DMSO-control. Data obtained on day 5 in triplicate, shown as mean ± SD. p values calculated by Mann-Whitney test.

(B) Bar chart showing percentage of co-expressing cells, determined by flow cytometry from two naive patient samples (BN46 and BN118) at the indicated time points of the treatment scheme: drug-on, exposure to vehicle (0.5% DMSO or 0.1% ethanol), or 500 μM TMZ, or 50 μM CCNU, or 10 μM dasatinib; drug-off, no drug exposure. Duplicate or triplicate data as mean ± SD. p values by Kruskal-Wallis with Dunn's post-hoc test.

(C) Flow cytometry profiling of KDM5B-expression in ALDH1A1+/pAKT+ cells. Data from genetically unmodified, naive patient samples BN46 (shown) and BN118 after exposure to TMZ (500 μM) -on/-off schedule as indicated.

(D) Protein expression patterns of PI3K-AKT-PTEN pathway genes subsequent to KDM5B knockdown by SMARTpool: ON-TARGETplus siRNA. Western Blot analysis of naive BN118 cells.

(E) Quantification data derived from quadruplicate western Blot analysis of naive patient samples BN46 and BN118. Treatment scheme as indicated. Data normalized as indicated and presented as mean ± SD.

(F) siKDM5B-knockdown/PTEN inhibitor-rescue experiment. Cartoon illustrates series of experiments conducted with naive patient samples BN46, BN118, E049, and E056. Bar plots present alamarBlue readout data, normalized to the corresponding siNT-controls and shown as mean ± SD. PTEN inhibition (PTENInh) by SF1670 (10 nM for 24 h).

(G) Caspase assay subsequent to indicated treatment scheme. Bar chart depicting MFI data of active caspase-3. Flow cytometry analysis of patient cell sample BN118 according to indicated treatment scheme. Data in triplicate as mean ± SD. p value by paired t-test.

(H) Caspase assay subsequent to indicated treatment schemes, involving TMZ (500 μM), CPI-455 (12 μM), or DMSO (0.5%). Left: Exemplary histograms, respectively color-coded. Bar chart depicting MFI data of active caspase-3. Flow cytometry analysis of patient cell sample BN118. Triplicate, data as mean ± SD. p values by paired t test.

Figure 2. *Continued*

(I) 12-day assays of indicated single- and combinatorial drug treatments, involving TMZ (500 μM), CPI-455 (12 μM), C46 (6 μM) or DMSO (0.5%). Bar plots represent alamarBlue cell viability readouts on naive patient samples BN46, and BN118, normalized to the DMSO-control. Duplicate/triplicate analysis, data as mean ± SD. p values by paired t test.

See also Figure S2 and Table S1.

mirror the composition of the top-ranked TMZ-rex BCIs (Figures 3H and S3F). This suggests that high individual levels of KDM5B in naive glioblastoma cells facilitate subclonal expansion in response to TMZ exposure. Separate analysis of treatment-naive KDM5B^{high} cells should therefore allow the prospective identification of the cellular origins to the dynamic drug resistant subclones driving disease progression.

DISCUSSION

The comparative study of paired tumor samples, derived from individuals at the time of initial diagnosis and at the time of disease relapse has shaped our basic understanding of the longitudinal molecular and cellular trajectories in glioblastoma.[8,30] Yet, we still do not understand glioblastoma progression. Particularly unclear is the dynamics of developing drug resistance, which occurs under the influence of guideline-based treatment with TMZ.[3] Contemporary research has revealed that the origins of this resistance may extend to early responses of heterogeneous tumor tissue to anticancer therapy. On a cellular level, this may affect resilient cells that are able to adapt immediately via non-genetic mechanisms and that then create progeny of expanding drug-resistant hierarchies (e.g.,[4,11,31]). Recent research of our lab has suggested that naive ALDH1A1+ cells in the primary tumor represent a candidate cellular source for this type of resistance in glioblastoma[5] and the present study has been conducted under the hypothesis that members of the KDM family of genes are early mediators of AKT-driven mechanisms in the process. Because heterogeneous patient-derived cellular models are suited to study subclonal enrichment *ex vivo*,[5,32] our current study took advantage of reductionist *in vitro* models to investigate the early steps of developing drug resistance.

Cellular assays, moreover, allow monitoring of dynamic processes, which cannot entirely be discovered when comparing only the starting vs. the endpoint of the course. In fact, the levels of KDM5B, as a key player during the process, appear unchanged in our investigated naive vs. post-TMZ clinical and experimental samples (see Figures S1B and S3D). In the vital cells, we instead observed that *KDM5B* expression increases immediately in the hierarchy of ALDH1A1+ cells upon TMZ exposure and, once triggered, it perpetuates for several days even without continuous therapeutic pressure. Presumably, this is the time during which TMZ resistant subclonal progression starts. Consequently, we observed KDM5B^{high} cells as a slow-cycling, but viable population under the influence of TMZ. This finding overlaps with the prevailing view that KDM5B links cellular transcriptomic heterogeneity to therapeutic resistance.[9,14,15]

An important aspect of our work relates to the predictability of adaptive/phenotypic plasticity. This feature is considered at the root of cellular heterogeneity and malignant disease progression, and it represents a newly recognized hallmark of cancer.[33] There is plenty of ongoing research striving to develop appropriate single-cell-based technologies and algorithms for the exposure of the respective malignant traits.[4,34,35] The use of vital clinical samples as a translational model could further this. Isolated tumor cells, organoids, or patient-derived tumor tissue explants are already considered as sophisticated future clinical decision tools, e.g., for predicting drug response.[32,36–39] In our present study, we relied on vital patient cells to screen for candidate genes and to subsequently investigate adaptive plasticity and subclonal dynamics in response to drug exposure in defined short-term assays. We used reporter-constructs, pharmacological and molecular interference as well as "unsupervised" barcode tracing to discover, model, and validate otherwise not accessible KDM5B-driven effects.

The clinical relatability of our research findings is the perspective of using KDM5B^{high} cells in the primary tumor tissue for predicting the occurrence of TMZ-resistant subclones in relapsing glioblastoma tissue, e.g., for use as a stratifying biomarker in future clinical trials. Our approach complements traditional computational ways to reconstruct the subclonal composition and evolution of cancer.[40–42] Because the derivation of tumor tissue from primary disease is a mandatory and preceding step to every primary treatment, short-term vital cell-based assays could find use as a companion diagnostic in the routine clinical care as well. The immediate dynamics of KDM5B could for example serve as a prospective indicator for accumulating TMZ-resistant subclones in the tissue of relapsing glioblastoma, which cannot always be surgically accessed. To promote exploratory findings beyond the preclinical stage, it is classically considered that clinical assay development and validation[43] as well as retrospective longitudinal and prospective screening must now be conducted.[44] If this succeeds, the dynamics of KDM5B^{high} cells could become a valid biomarker for sequential therapies targeting the accumulation of drug resistant subclones during disease progression. This would represent a valuable alternative—in an era in which the static O(6)-methylguanine-DNA methyltransferase (*MGMT*) promoter methylation status is still the single most important prognostic and predictive factor for TMZ-based guideline-oriented chemotherapy of glioblastoma.[3,45]

Limitations of the study

The exact mechanism underlying our observations still remains to be determined. Our data indicate, similar as described in hepatocellular cancer,[16] that KDM5B decreases PTEN to activate AKT and downstream effector signaling in naive tumor cells, independent of the many ways that subsequent TMZ exposure could interfere with in this signaling cascade or with other resistance-related pathways.[46,47] We could not reveal an interaction with PI3K as described for prostate or oral cancers.[24,48] We therefore speculated on an epigenetic route, but we could not reveal a direct demethylation activity on key players in the pathway either—at least not by studying the overall population of cells. Notably, KDM5B^{high} cells (the top 5% of KDM5B-expressing cells) represent a rare phenotype among naive glioblastoma cells. It is possible that direct biochemical evidence linking KDM5B-dependent lysine demethylation with AKT signaling could only be revealed via H3K4me3
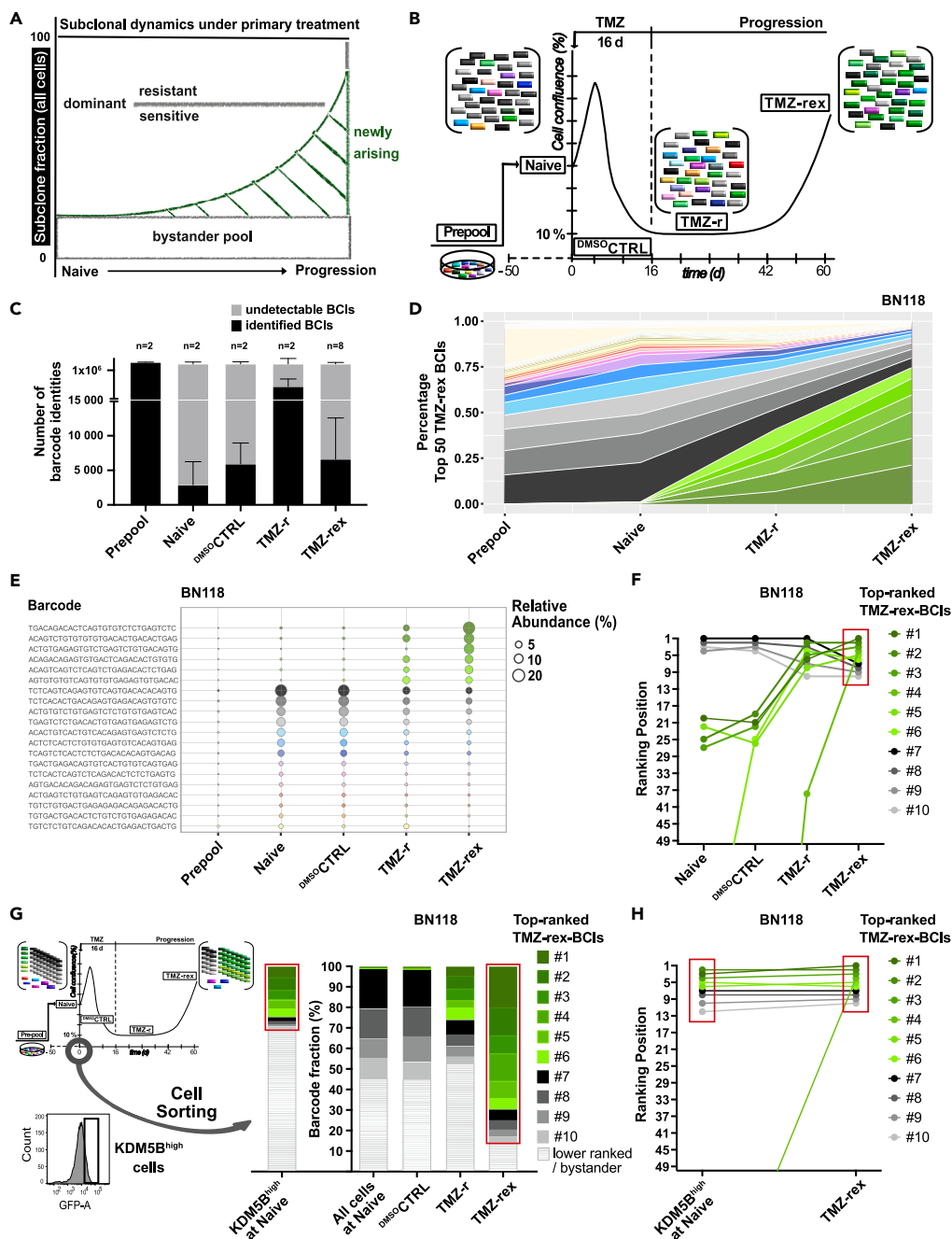
Figure 3. KDM5B expression predicts TMZ-triggered subclonal growth

(A) Working model. Subclonal dynamics occurs under therapeutic pressure of primary treatment. It results from shifting abundance of treatment-resistant vs. treatment-sensitive cellular hierarchies. Some hierarchies dominate at the naive stage, others appear to arise newly under drug exposure. A bystander pool of cells does not participate in the dynamic course of subclones.

(B) Cartoon illustrating the experimental barcoding setup. Naive BN46 and BN118 patient cells were provided with the ClonTracer barcoding construct,[28] exposed to 500 μM TMZ or 0.5% DMSO, and analyzed by NGS at the indicated time points. TMZ-resistant cells, TMZ-r; expanding TMZ-resistant cells, TMZ-rex.

(C) NGS-based quantification of detectable barcode identities (BCIs) from (B). Bar charts representing ratios of identifiable vs. undetectable BCIs at the indicated experimental stages. Data points from naive patient samples BN46 and BN118, presented as mean ± SD. (D–H) Note: green-scale, newly arising BCIs under TMZ exposure vs. gray-scale, dominant BCIs at the *Naive* stage of the experiment. Data from patient sample BN118.

(D) Subclonal dynamics from (B), visualized as a stacked plot. Data represent the relative frequencies of the top 50 BCIs, as defined at the TMZ-rex stage, displayed for each stage of the experiments.

Figure 3. *Continued*

(E) Subclonal dynamics from (B), visualized as a bubble plot. Data represent relative barcode abundances, barcode identity as specified, at the indicated time points of the experiments. Barcodes of at least 1% relative abundance shown.

(F) Subclonal dynamics from (B), visualized as a ranked plot. Data represent individual ranking positions of the top 10 BCIs, as defined at the TMZ-rex stage, displayed for each stage of the experiments.

(G) Sorting experiment. Cartoon illustrating cell sorting of KDM5B^{high} barcoded cells at the *Naive* stage of the experiment. Subclonal dynamics and top TMZ-rex can be predicted; visualized as a slice plot (red boxes). Data represent ranking positions of the top 10 BCIs, as defined at the TMZ-rex stage, color-coded for identity and displayed in relative abundance for each stage of the experiment. Abundance of lower-ranked thousands of bystander identities in white.

(H) Subclonal dynamics and top TMZ-rex can be predicted; visualized as a ranked plot (red boxes). Data represent individual ranking positions of the top 10 BCIs, as defined at the TMZ-rex stage, color-coded for identity and displayed as ranking positions at the TMZ-rex stage and for the *Naive*-sorted KDM5B^{high} cells. Note the similarity of ranking positions among the individual BCIs at both time points.

See also Figure S3 and Table S1.

ChiP-seq and RNA-seq analysis in this limited population of cells, which should be addressed in future work. Also, KDM5B could act indirectly, e.g., via genomic instability control,[49] regulation of cell cycle progression,[15,50] or by interactions with other chromatin regulators.[51–53] Alternative pathways may additionally be involved, such as signaling by c-Met, p16/Ink4a, Wnt/β-catenin, or FBXW7/CCNE1,[54–57] which remains to be further elucidated for the TMZ-induced hierarchy of ALDH1A1+ glioblastoma cells. In all, our study demonstrates, by use of patient-derived cellular models, the predictability of subclonal enrichment under defined primary drug exposure. Clinical translation of these findings will require appropriate assay development and longitudinal, prospective trial designs.

STAR★METHODS

Detailed methods are provided in the online version of this paper and include the following:

- KEY RESOURCES TABLE
- RESOURCE AVAILABILITY
  - Lead contact
  - Materials availability
  - Data and code availability
- EXPERIMENTAL MODEL AND STUDY PARTICIPANT DETAILS
- METHOD DETAILS
  - Transduction of KDM5B-EGFP-reporter construct
  - Cellular assays
  - Experimental readouts
  - Barcoding of glioblastoma patient cells
- QUANTIFICATION AND STATISTICAL ANALYSIS

SUPPLEMENTAL INFORMATION

Supplemental information can be found online at https://doi.org/10.1016/j.isci.2023.108596.

AUTHOR CONTRIBUTIONS

V.U., data curation, formal analysis, investigation, visualization, methodology, writing – original draft and editing. S.E., data curation, formal analysis, investigation, visualization. A.B., data curation, formal analysis, investigation, visualization. M.D., methodology, formal analysis, supervision. H.H.G., data curation, formal analysis, visualization. I.C., formal analysis, visualization. P.B., data curation, formal analysis, visualization. C.D., data curation, formal analysis, visualization. S.L., data curation, investigation, visualization. L.M., data curation, visualization. P.D., formal analysis, visualization. S.K., formal analysis, resources. M.G., resources. T.B., resources. K.K., resources. L.R., methodology, resources.

U.S., conceptualization, resources. A.R., methodology, conceptualization, resources. B.M.G., conceptualization, formal analysis, supervision, resources, methodology, writing – review and editing. B.S., conceptualization, formal analysis, supervision, funding acquisition, methodology, writing – original draft, writing – review and editing, project administration.

DECLARATION OF INTERESTS

The authors declare no conflicts of interest.

INCLUSION AND DIVERSITY

We support inclusive, diverse, and equitable conduct of research.

SUPPORTING CITATIONS

The following reference appears in the supplemental information: 59.

REFERENCES

1. Chen, J., Li, Y., Yu, T.S., McKay, R.M., Burns, D.K., Kernie, S.G., and Parada, L.F. (2012). A restricted cell population propagates glioblastoma growth after chemotherapy. Nature 488, 522–526.

2. Lan, X., Jörg, D.J., Cavalli, F.M.G., Richards, L.M., Nguyen, L.V., Vanner, R.J., Guilhamon, P., Lee, L., Kushida, M.M., Pellacani, D., et al. (2017). Fate mapping of human glioblastoma reveals an invariant stem cell hierarchy. Nature 549, 227–232.

3. Weller, M., van den Bent, M., Preusser, M., Le Rhun, E., Tonn, J.C., Minniti, G., Bendszus, M., Balana, C., Chinot, O., Dirven, L., et al. (2021). EANO guidelines on the diagnosis and treatment of diffuse gliomas of adulthood. Nat. Rev. Clin. Oncol. 18, 170–186.

4. Gimple, R.C., Yang, K., Halbert, M.E., Agnihotri, S., and Rich, J.N. (2022). Brain cancer stem cells: resilience through adaptive plasticity and hierarchical heterogeneity. Nat. Rev. Cancer 22, 497–514.

5. Kebir, S., Ullrich, V., Berger, P., Dobersalske, C., Langer, S., Rauschenbach, L., Trageser, D., Till, A., Lorbeer, F.K., Wieland, A., et al. (2023). A Sequential Targeting Strategy Interrupts AKT-Driven Subclone-Mediated Progression in Glioblastoma. Clin. Cancer Res. 29, 488–500.

6. Eyler, C.E., Matsunaga, H., Hovestadt, V., Vantine, S.J., van Galen, P., and Bernstein, B.E. (2020). Single-cell lineage analysis reveals genetic and epigenetic interplay in glioblastoma drug resistance. Genome Biol. 21, 174.

7. Barthel, F.P., Johnson, K.C., Varn, F.S., Moskalik, A.D., Tanner, G., Kocakavuk, E., Anderson, K.J., Abiola, O., Aldape, K., Alfaro, K.D., et al. (2019). Longitudinal molecular trajectories of diffuse glioma in adults. Nature 576, 112–120.

8. Korber, V., Yang, J., Barah, P., Wu, Y., Stichel, D., Gu, Z., Fletcher, M.N.C., Jones, D., Hentschel, B., Lamszus, K., et al. (2019). Evolutionary Trajectories of IDH(WT) Glioblastomas Reveal a Common Path of Early Tumorigenesis Instigated Years ahead of Initial Diagnosis. Cancer Cell 35, 692–704.e12.

9. Roesch, A., Fukunaga-Kalabis, M., Schmidt, E.C., Zabierowski, S.E., Brafford, P.A., Vultur, A., Basu, D., Gimotty, P., Vogt, T., and Herlyn, M. (2010). A temporally distinct subpopulation of slow-cycling melanoma cells is required for continuous tumor growth. Cell 141, 583–594.

10. Sharma, S.V., Lee, D.Y., Li, B., Quinlan, M.P., Takahashi, F., Maheswaran, S., McDermott, U., Azizian, N., Zou, L., Fischbach, M.A., et al. (2010). A chromatin-mediated reversible drug-tolerant state in cancer cell subpopulations. Cell 141, 69–80.

11. Marine, J.C., Dawson, S.J., and Dawson, M.A. (2020). Non-genetic mechanisms of therapeutic resistance in cancer. Nat. Rev. Cancer 20, 743–756.

12. Shen, S., Vagner, S., and Robert, C. (2020). Persistent Cancer Cells: The Deadly Survivors. Cell 183, 860–874.

13. Banelli, B., Carra, E., Barbieri, F., Würth, R., Parodi, F., Pattarozzi, A., Carosio, R., Forlani, A., Allemanni, G., Marubbi, D., et al. (2015). The histone demethylase KDM5A is a key factor for the resistance to temozolomide in glioblastoma. Cell Cycle 14, 3418–3429.

14. Banelli, B., Daga, A., Forlani, A., Allemanni, G., Marubbi, D., Pistillo, M.P., Profumo, A., and Romani, M. (2017). Small molecules targeting histone demethylase genes (KDMs) inhibit growth of temozolomide-resistant glioblastoma cells. Oncotarget 8, 34896–34910.

15. Dai, B., Hu, Z., Huang, H., Zhu, G., Xiao, Z., Wan, W., Zhang, P., Jia, W., and Zhang, L. (2014). Overexpressed KDM5B is associated with the progression of glioma and promotes glioma cell growth via downregulating p21. Biochem. Biophys. Res. Commun. 454, 221–227.

16. Fang, L., Zhao, J., Wang, D., Zhu, L., Wang, J., and Jiang, K. (2016). Jumonji AT-rich interactive domain 1B overexpression is associated with the development and progression of glioma. Int. J. Mol. Med. 38, 172–182.

17. Romani, M., Daga, A., Forlani, A., Pistillo, M.P., and Banelli, B. (2019). Targeting of Histone Demethylases KDM5A and KDM6B Inhibits the Proliferation of Temozolomide-Resistant Glioblastoma Cells. Cancers 11, 878.

18. Liau, B.B., Sievers, C., Donohue, L.K., Gillespie, S.M., Flavahan, W.A., Miller, T.E., Venteicher, A.S., Hebert, C.H., Carey, C.D., Rodig, S.J., et al. (2017). Adaptive Chromatin Remodeling Drives Glioblastoma Stem Cell Plasticity and Drug Tolerance. Cell Stem Cell 20, 233–246.e7.

19. Glas, M., Happold, C., Rieger, J., Wiewrodt, D., Bähr, O., Steinbach, J.P., Wick, W., Kortmann, R.D., Reifenberger, G., Weller, M., and Herrlinger, U. (2009). Long-term survival of patients with glioblastoma treated with radiotherapy and lomustine plus temozolomide. J. Clin. Oncol. 27, 1257–1261.

20. Wick, W., Gorlia, T., Bendszus, M., Taphoorn, M., Sahm, F., Harting, I., Brandes, A.A., Taal, W., Domont, J., Idbaih, A., et al. (2017). Lomustine and Bevacizumab in Progressive Glioblastoma. N. Engl. J. Med. 377, 1954–1963.

21. Roesch, A., Vultur, A., Bogeski, I., Wang, H., Zimmermann, K.M., Speicher, D., Körbel, C., Laschke, M.W., Gimotty, P.A., Philipp, S.E., et al. (2013). Overcoming intrinsic multidrug resistance in melanoma by blocking the mitochondrial respiratory chain of slow-cycling JARID1B(high) cells. Cancer Cell 23, 811–825.

22. Hinohara, K., Wu, H.J., Vigneau, S., McDonald, T.O., Igarashi, K.J., Yamamoto, K.N., Madsen, T., Fassl, A., Egri, S.B., Papanastasiou, M., et al. (2018). KDM5 Histone Demethylase Activity Links Cellular Transcriptomic Heterogeneity to Therapeutic Resistance. Cancer Cell 34, 939–953.e9.

23. Tang, B., Qi, G., Tang, F., Yuan, S., Wang, Z., Liang, X., Li, B., Yu, S., Liu, J., Huang, Q., et al. (2015). JARID1B promotes metastasis and epithelial-mesenchymal transition via PTEN/AKT signaling in hepatocellular carcinoma cells. Oncotarget 6, 12723–12739.

24. Li, G., Kanagasabai, T., Lu, W., Zou, M.R., Zhang, S.M., Celada, S.I., Izban, M.G., Liu, Q., Lu, T., Ballard, B.R., et al. (2020). KDM5B Is Essential for the Hyperactivation of PI3K/AKT Signaling in Prostate Tumorigenesis. Cancer Res. 80, 4633–4643.

25. Rosivatz, E., Matthews, J.G., McDonald, N.Q., Mulet, X., Ho, K.K., Lossi, N., Schmid, A.C., Mirabelli, M., Pomeranz, K.M., Erneux, C., et al. (2006). A small molecule inhibitor for phosphatase and tensin homologue deleted on chromosome 10 (PTEN). ACS Chem. Biol. 1, 780–790.

26. Fu, Y.D., Huang, M.J., Guo, J.W., You, Y.Z., Liu, H.M., Huang, L.H., and Yu, B. (2020). Targeting histone demethylase KDM5B for cancer treatment. Eur. J. Med. Chem. 208, 112760.

27. Liang, J., Zhang, B., Labadie, S., Ortwine, D.F., Vinogradova, M., Kiefer, J.R., Gehling, V.S., Harmange, J.C., Cummings, R., Lai, T., et al. (2016). Lead optimization of a pyrazolo [1,5-a]pyrimidin-7(4H)-one scaffold to identify potent, selective and orally bioavailable KDM5 inhibitors suitable for in vivo biological studies. Bioorg. Med. Chem. Lett. 26, 4036–4041.

28. Bhang, H.e.C., Ruddy, D.A., Krishnamurthy Radhakrishna, V., Caushi, J.X., Zhao, R., Hims, M.M., Singh, A.P., Kao, I., Rakiec, D., Shaw, P., et al. (2015). Studying clonal dynamics in response to cancer therapy using high-complexity barcoding. Nat. Med. 21, 440–448.

29. Howland, K.K., and Brock, A. (2023). Cellular barcoding tracks heterogeneous clones through selective pressures and phenotypic transitions. Trends Cancer 9, 591–601.

30. Schäfer, N., Gielen, G.H., Rauschenbach, L., Kebir, S., Till, A., Reinartz, R., Simon, M., Niehusmann, P., Kleinschnitz, C., Herrlinger, U., et al. (2019). Longitudinal heterogeneity in glioblastoma: moving targets in recurrent versus primary tumors. J. Transl. Med. 17, 96.

31. Shaffer, S.M., Dunagin, M.C., Torborg, S.R., Torre, E.A., Emert, B., Krepler, C., Beqiri, M., Sproesser, K., Brafford, P.A., Xiao, M., et al. (2017). Rare cell variability and drug-induced reprogramming as a mode of cancer drug resistance. Nature 546, 431–435.

32. Reinartz, R., Wang, S., Kebir, S., Silver, D.J., Wieland, A., Zheng, T., Küpper, M., Rauschenbach, L., Fimmers, R., Shepherd, T.M., et al. (2017). Functional Subclone Profiling for Prediction of Treatment-Induced Intratumor Population Shifts and Discovery of Rational Drug Combinations in Human Glioblastoma. Clin. Cancer Res. 23, 562–574.

33. Hanahan, D. (2022). Hallmarks of Cancer: New Dimensions. Cancer Discov. 12, 31–46.

34. Rambow, F., Rogiers, A., Marin-Bejar, O., Aibar, S., Femel, J., Dewaele, M., Karras, P., Brown, D., Chang, Y.H., Debiec-Rychter, M., et al. (2018). Toward Minimal Residual Disease-Directed Therapy in Melanoma. Cell 174, 843–855.e19.

35. Burkhardt, D.B., San Juan, B.P., Lock, J.G., Krishnaswamy, S., and Chaffer, C.L. (2022). Mapping Phenotypic Plasticity upon the Cancer Cell State Landscape Using Manifold Learning. Cancer Discov. 12, 1847–1859.

36. Lee, J., Kotliarova, S., Kotliarov, Y., Li, A., Su, Q., Donin, N.M., Pastorino, S., Purow, B.W., Christopher, N., Zhang, W., et al. (2006). Tumor stem cells derived from glioblastomas cultured in bFGF and EGF more closely mirror the phenotype and genotype of primary tumors than do serum-cultured cell lines. Cancer Cell 9, 391–403.

37. Drost, J., and Clevers, H. (2018). Organoids in cancer research. Nat. Rev. Cancer 18, 407–418.

38. Sood, D., Tang-Schomer, M., Pouli, D., Mizzoni, C., Raia, N., Tai, A., Arkun, K., Wu, J., Black, L.D., 3rd, Scheffler, B., et al. (2019). 3D extracellular matrix microenvironment in bioengineered tissue models of primary pediatric and adult brain tumors. Nat. Commun. 10, 4529.

39. Voabil, P., de Bruijn, M., Roelofsen, L.M., Hendriks, S.H., Brokamp, S., van den Braber, M., Broeks, A., Sanders, J., Herzig, P., Zippelius, A., et al. (2021). An ex vivo tumor fragment platform to dissect response to PD-1 blockade in cancer. Nat. Med. 27, 1250–1261.

40. Chowell, D., Napier, J., Gupta, R., Anderson, K.S., Maley, C.C., and Sayres, M.A.W. (2018). Modeling the Subclonal Evolution of Cancer Cell Populations. Cancer Res. 78, 830–839.

41. Tarabichi, M., Salcedo, A., Deshwar, A.G., Ni Leathlobhair, M., Wintersinger, J., Wedge, D.C., Van Loo, P., Morris, Q.D., and Boutros, P.C. (2021). A practical guide to cancer subclonal reconstruction from DNA sequencing. Nat. Methods 18, 144–155.

42. Dentro, S.C., Leshchiner, I., Haase, K., Tarabichi, M., Wintersinger, J., Deshwar, A.G., Yu, K., Rubanova, Y., Macintyre, G., Demeulemeester, J., et al. (2021). Characterizing genetic intra-tumor heterogeneity across 2,658 human cancer genomes. Cell 184, 2239–2254.e39.

43. Wu, L., and Qu, X. (2015). Cancer biomarker detection: recent achievements and challenges. Chem. Soc. Rev. 44, 2963–2997.

44. Pepe, M.S., Etzioni, R., Feng, Z., Potter, J.D., Thompson, M.L., Thornquist, M., Winget, M., and Yasui, Y. (2001). Phases of biomarker development for early detection of cancer. J. Natl. Cancer Inst. 93, 1054–1061.

45. Hegi, M.E., Diserens, A.C., Gorlia, T., Hamou, M.F., de Tribolet, N., Weller, M., Kros, J.M., Hainfellner, J.A., Mason, W., Mariani, L., et al. (2005). MGMT gene silencing and benefit from temozolomide in glioblastoma. N. Engl. J. Med. 352, 997–1003.

46. Ortiz, R., Perazzoli, G., Cabeza, L., Jiménez-Luna, C., Luque, R., Prados, J., and Melguizo, C. (2021). Temozolomide: An Updated Overview of Resistance Mechanisms, Nanotechnology Advances and Clinical Applications. Curr. Neuropharmacol. 19, 513–537.

47. Singh, N., Miner, A., Hennis, L., and Mittal, S. (2021). Mechanisms of temozolomide resistance in glioblastoma - a comprehensive review. Cancer Drug Resist. 4, 17–43.

48. Facompre, N.D., Harmeyer, K.M., Sole, X., Kabraji, S., Belden, Z., Sahu, V., Whelan, K., Tanaka, K., Weinstein, G.S., Montone, K.T., et al. (2016). JARID1B Enables Transit between Distinct States of the Stem-like Cell Population in Oral Cancers. Cancer Res. 76, 5538–5549.

49. Li, X., Liu, L., Yang, S., Song, N., Zhou, X., Gao, J., Yu, N., Shan, L., Wang, Q., Liang, J., et al. (2014). Histone demethylase KDM5B is a key regulator of genome stability. Proc. Natl. Acad. Sci. USA 111, 7096–7101.

50. Mitra, D., Das, P.M., Huynh, F.C., and Jones, F.E. (2011). Jumonji/ARID1 B (JARID1B) protein promotes breast tumor cell cycle progression through epigenetic repression of microRNA let-7e. J. Biol. Chem. 286, 40531–40535.

51. Li, Q., Shi, L., Gui, B., Yu, W., Wang, J., Zhang, D., Han, X., Yao, Z., and Shang, Y. (2011). Binding of the JmjC demethylase JARID1B to LSD1/NuRD suppresses angiogenesis and metastasis in breast cancer cells by repressing chemokine CCL14. Cancer Res. 71, 6899–6908.

52. Zhang, Y., Liang, J., and Li, Q. (2014). Coordinated regulation of retinoic acid signaling pathway by KDM5B and polycomb repressive complex 2. J. Cell. Biochem. 115, 1528–1538.

53. Zhang, S.M., Cai, W.L., Liu, X., Thakral, D., Luo, J., Chan, L.H., McGeary, M.K., Song, E., Blenman, K.R.M., Micevic, G., et al. (2021). KDM5B promotes immune evasion by recruiting SETDB1 to silence retroelements. Nature 598, 682–687.

54. Ohta, K., Haraguchi, N., Kano, Y., Kagawa, Y., Konno, M., Nishikawa, S., Hamabe, A., Hasegawa, S., Ogawa, H., Fukusumi, T., et al. (2013). Depletion of JARID1B induces cellular senescence in human colorectal cancer. Int. J. Oncol. 42, 1212–1218.

55. Kuo, K.T., Huang, W.C., Bamodu, O.A., Lee, W.H., Wang, C.H., Hsiao, M., Wang, L.S., and Yeh, C.T. (2018). Histone demethylase JARID1B/KDM5B promotes aggressiveness of non-small cell lung cancer and serves as a good prognostic predictor. Clin. Epigenetics 10, 107.

56. Huang, D., Xiao, F., Hao, H., Hua, F., Luo, Z., Huang, Z., Li, Q., Chen, S., Cheng, X., Zhang, X., et al. (2020). JARID1B promotes colorectal cancer proliferation and Wnt/beta-catenin signaling via decreasing CDX2 level. Cell Commun. Signal. 18, 169.

57. Chen, B., Chen, H., Lu, S., Zhu, X., Que, Y., Zhang, Y., Huang, J., Zhang, L., Zhang, Y., Sun, F., et al. (2022). KDM5B promotes tumorigenesis of Ewing sarcoma via FBXW7/CCNE1 axis. Cell Death Dis. 13, 354.

58. Louis, D.N., Perry, A., Wesseling, P., Brat, D.J., Cree, I.A., Figarella-Branger, D., Hawkins, C., Ng, H.K., Pfister, S.M., Reifenberger, G., et al. (2021). The 2021 WHO Classification of Tumors of the Central Nervous System: a summary. Neuro Oncol. 23, 1231–1251.

59. Buehler, E., Chen, Y.C., and Martin, S. (2012). C911: A bench-level control for sequence specific siRNA off-target effects. PLoS One 7, e51942.

60. Vinogradova, M., Gehling, V.S., Gustafson, A., Arora, S., Tindell, C.A., Wilson, C., Williamson, K.E., Guler, G.D., Gangurde, P., Manieri, W., et al. (2016). An inhibitor of KDM5 demethylases reduces survival of drug-tolerant cancer cells. Nat. Chem. Biol. 12, 531–538.

STAR★METHODS

KEY RESOURCES TABLE

REAGENT or RESOURCE	SOURCE	IDENTIFIER
Antibodies		
Active Caspase-3 (FITC) (Clone: C92-605)	BD Biosciences	Cat#559341; RRID: AB_397234
ALDH1A1 (FITC)	Abcam	Cat#ab275646; RRID: N/A
Cyclin D3	Cell signaling	Cat#2936, RRID: AB_2070801
Histone H3 (tri methyl K4) antibody - ChIP Grade	Abcam	Cat#ab8580; RRID:AB_306649
Human Fc Block	BD Biosciences	Cat#564220, RRID: AB_2869554
KDM5B	Novus	Cat#NB100-97821; RRID: AB_1291176
KDM5B	Sigma-Aldrich	Cat#HPA027179, RRID: AB_1851987
phospho-AKT (Ser473) (Alexa488)	BD Biosciences	Cat#560404; RRID: AB_1645342
phospho-AKT (Ser473) XP®	Cell signaling	Cat#4060S, RRID: AB_2315049
phospho-GSK3ß (Ser9)	Cell signaling	Cat#5558P, RRID: AB_10013750
phospho-mTOR (Ser2448) XP®	Cell signaling	Cat#5536P, RRID: AB_10691552
PI3 Kinase p85	Cell signaling	Cat#4292; RRID: AB_329869
PI3 Kinase p110α	Cell signaling	Cat#4255; RRID: AB_659888
secondary antibody Alexa-Fluor 555 (goat anti-rabbit IgG)	Thermo Fisher Scientific	Cat#A21428; RRID: AB_2535849
secondary antibody Alexa-Fluor 647 (donkey anti-rabbit IgG)	BioLegend	Cat#406414, RRID:AB_2563202
secondary antibody HRP-linked (Anti-rabbit IgG)	Cell signaling	Cat#7074, RRID: AB_2099233
secondary antibody HRP-linked (Anti-mouse IgG)	Cell signaling	Cat#7076, RRID: AB_330924
β-actin	Sigma-Aldrich	Cat#A5441, RRID: AB_476744
Chemicals, peptides, and recombinant proteins		
C46	Genentech	This paper; N/A
CPI-455	Selleckchem	Cat#S8287
SF1670	Selleckchem	Cat#S7310
TMZ	Sigma-Aldrich	Cat#PHR1437
DMSO	Sigma-Aldrich	Cat#D2650
Critical commercial assays		
CellTrace™ Far Red solution	Thermo Fischer	Cat#C34572
BD Cytofix/Cytoperm™ Fixation/Permeabilization Kit	BD Biosciences	Cat#554714; RRID: AB_2869008
alamarBlue™ assay	Life Technologies	Cat# DAL 1100
Oligonucleotides		
ON-TARGETplus Non-targeting Pool (5 nmol)	Horizon Discovery	D-001810-10-05
ON-TARGETplus KDM5B siRNA (5 nmol)	Horizon Discovery	L-009899-00-0005
ON-TARGETplus set of 4 siRNAs (Target Sequence 1: GGAGAUGCACUUCGAUAUA)	Horizon Discovery	LQ-009899-00-0005
C911 siRNA 1: GGAGAUGCUGAUCGAUAUA	Horizon Discovery	N/A
ON-TARGETplus set of 4 siRNAs (Target Sequence 2: UAAGUUAGUUGCAGAAGAA)	Horizon Discovery	N/A
C911 siRNA 2: UAAGUUAGAACCAGAAGAA	Horizon Discovery	N/A
ON-TARGETplus set of 4 siRNAs (Target Sequence 3: UCGAAGAGAUCCCUGCAUA)	Horizon Discovery	N/A
C911 siRNA 3: UCGAAGAGUAGCCUGCAUA	Horizon Discovery	N/A

(Continued on next page)

Continued

REAGENT or RESOURCE	SOURCE	IDENTIFIER
ON-TARGETplus set of 4 siRNAs (Target Sequence 4: GGAAGAUCUUGGACUUAUU	Horizon Discovery	N/A
C911 siRNA 4: GGAAGAUCAACGACUUAUU	Horizon Discovery	N/A
Primer: ALDH1A1 Fw: GCACGCCAGACTT ACCTGTC, Rv: CCTCCTCAGTTGCAGGATTAAAG	IDT	N/A
Primer: KDM1A Fw: TGACCGGATGACTTCTCAAGA, Rv: GTTGGAGAGTAGCCTCAAATGTC	Eurofins	N/A
Primer: KDM1B Fw: CTCTCCTGTGGGGAACATTTC, Rv: GACTAGGTTCGGTTTTGCCATT	Eurofins	N/A
Primer: KDM2B Fw: GGGTTCCCCTGATATTTCGAGA, Rv: GCTCCCCACTAGGAGTTTGAC	Eurofins	N/A
Primer: KDM5A Fw: GTCACCTGGAGCTAAGGCAC, Rv: CCGTTTCCGTTTCTTCTCTG	IDT	N/A
Primer: KDM5B Fw: AGTGGGCTCACATATCAGAGG, Rv: CAAACACCTTAGGCTGTCTCC	IDT	N/A
Primer: KDM5C Fw: CTTGCTACGCTCCCACTACG, Rv: TGTGTTACACTGCACAAGGTTG	Eurofins	N/A
Primer: KDM5D Fw: CAAGACCCGCTTGGCTACATT, Rv: TTGGACGCGAGGAGTAAATCT	Eurofins	N/A
Primer: KDM6A Fw: TACAGGCTCAGTTGTGTAACCT, Rv: CTGCGGGAATTGGTAGGCTC	IDT	N/A
Primer: RPL37A Fw: GACGTACAATACCACTTCCGC, Rv: GGAGCGTCTACTGGTCTTTCA	IDT	N/A
Barcoding Index Primer: Fw: AATGATACGGCGACCAC CGAGATCTACACACTGACTGCAGTCTGAGTCTGACAG; Rv: CAAGCAGAAGACGGCATACGAGAT - (index of 6 bases) -GTGACTGGAGTTCAGACGTGTGC TCTTCCGATCTCTAGCATAGAGTGCGTAGCTCTGCT.	Eurofins	N/A
Custom Primer Illumina Sequencing: (5'-3') ACACACT GACTGCAGTCTGAGTCTGACA	Eurofins	N/A
Recombinant DNA		
ClonTracer library	Addgene	Cat#67267; RRID: Addgene_67267
pCMV delta R8.2	Addgene	Cat #12263; RRID: Addgene_12263
pCMV-VSV-G	Addgene	Cat #8454; RRID: Addgene_8454
pLU-JARID1Bprom-EGFP-BLAST	Roesch et al.[9]	
pMD2.G	Addgene	Cat #12259; RRID: Addgene_12259
pMDLg/pRRE	Addgene	Cat #12251; RRID: Addgene_12251
pRSV-Rev	Addgene	Cat #12253; RRID: Addgene_12253
Software and algorithms		
FACS Diva software version v8.0.1.1	BD Biosciences	URL: https://www.bdbiosciences.com/en-ca/products/instruments/software-informatics/instrument-software/bd-facsdiva-software
FlowJo software v10.5.3	BD Biosciences	URL: https://www.flowjo.com/solutions/flowjo/downloads
GraphPad Prism v8	GraphPad Software Inc.	URL: https://www.graphpad.com/features
Image Lab™ software v6.0.1	BioRad	URL: https://www.bio-rad.com/de-de/product/image-lab-software?ID=KRE6P5E8Z
Python v3.9.9	Python Software Foundation	URL: https://www.python.org/downloads/

Continued

REAGENT or RESOURCE	SOURCE	IDENTIFIER
R software v4.2.2	Posit PBC	URL: https://cran.utstat.utoronto.ca/ and https://posit.co/download/rstudio-desktop/
Illumina bcl2fastq 2.20.0.422 Conversion Software		URL: https://support.illumina.com/sequencing/sequencing_software/bcl2fastq-conversion-software.html

RESOURCE AVAILABILITY

Lead contact

Further information and requests for resources and reagents should be directed to and will be fulfilled by the lead contact, Björn Scheffler (b.scheffler@dkfz-heidelberg.de).

Materials availability

This study did not generate new unique reagents.

Data and code availability

All data reported in this paper will be shared by the lead contact upon request.

This paper does not report original code.

Any additional information required to reanalyze the data reported in this paper is available from the lead contact upon request.

EXPERIMENTAL MODEL AND STUDY PARTICIPANT DETAILS

Pairs of vital patient cells representing treatment-naive and TMZ pre-exposed relapse samples, were derived as reported previously[5] from clinical *IDH*-wt glioblastoma tissue at the University Bonn Medical Center (sample IDs: BN; n=6 patients) (Table S1). All studies were conducted in accordance with recognized ethical guidelines (Declaration of Helsinki) and approved by the respective local ethics committees (institutional review boards); all patients provided informed written consent. Tumor classification relied on the 2021 WHO guidelines[58] and was provided by routine neuropathology methods. Patient cell samples, regularly polymerase chain reaction (PCR)-tested negative for mycoplasm, were used at passages 5-18 for *in vitro* experimentation. Sample authentication was conducted by STR analysis. Culture conditions included Neurobasal-media supplemented with 1% Glutamin, 1% B27 Supplement, 1% Antibiotic- Antimycotic, 0.5% N2 Supplement and 1μg/ml Laminin, supplemented with 10ng/mL EGF and bFGF every 48 hours. Cells were grown in Laminin/Poly-L-ornithine coated plasticware. Unless otherwise specified, media, reagents, and analytical compounds were obtained from Life Technologies (Carlsbad, CA, USA) or Sigma-Aldrich (St. Louis, MO, USA).

METHOD DETAILS

Transduction of KDM5B-EGFP-reporter construct

The KDM5B-promoter-EGFP-reporter construct was stably integrated into early passage (p4-p13) naive BN46, BN118, E049, E056, as well as TMZ-exposed [TMZ→eR]BN46, [cR]BN118 patient cell samples via lentiviral infection. Lentivirus was produced in HEK293T cells using the TransIT-TKO® transfection reagent Mirus (Mirus Bio; Madison, Wisconsin, USA), Opti-MEM™ Reduced Serum Medium (Thermo Fisher Scientific; Waltham, MA, USA) and the following plasmids: 2.5μg Lenti (pLU-JARID1Bprom-EGFP-BLAST; from[9]), 2.5μg pMDLg/pRRE (Addgene, Watertown, MA, USA #12251; RRID: Addgene_12251), 2.5μg pRSV-Rev (Addgene #12253; RRID: Addgene_12253); 2.5μg pMD2.G (Addgene #12259; RRID: Addgene_12259). For stable transduction, 10^6 cells of the indicated patient cell samples were provided with virus for 48 hours and selection of cells was achieved by blasticidin (Invivogen; San Diego, California, USA) and confirmed using flow cytometry for EGFP. The transduced cells were expanded under controlled culture conditions for 2-4 passages, frozen as stocks, thawed and passaged once more for consecutive experimentation.

Cellular assays

A schematic representation of individual experimental settings and workflows is provided for each long-term or reductionist cellular assay.

For drug exposure studies, indicated vital cells were seeded 24 hours prior to the experiment. Compounds were provided as a single dose (SF1670, 10nM; Selleckchem; Houston, TX, USA) or every other day (TMZ, 500μM, Sigma-Aldrich; CPI-455, 12μM, Selleckchem, according to[14,60]; C46, 6μM, kindly provided by Genentech as part of an institutional MTA (ID: OR-216374); DMSO in corresponding concentrations, Sigma-Aldrich).

For knockdown studies, the following siRNAs were used (20μM, each): SMARTpool: ON-TARGETplus KDM5B siRNA (5nmol; L-009899-00-0005) and ON-TARGETplus Non-targeting Pool (nmol; D-001810-10-05), both Horizon Discovery (Waterbeach, UK). In addition to this the

following individual single siRNAs (ON-TARGETplus set of 4 KDM5B siRNAs) and corresponding C911 controls were used, all Horizon Discovery (Waterbeach, UK):

Target Sequence 1: GGAGAUGCACUUCGAUAUA;
C911 siRNA 1: GGAGAUGCUGAUCGAUAUA;
Target Sequence 2: UAAGUUAGUUGCAGAAGAA;
C911 siRNA 2: UAAGUUAGAACCAGAAGAA;
Target Sequence 3: UCGAAGAGAUCCCUGCAUA;
C911 siRNA 3: UCGAAGAGUAGCCUGCAUA;
Target Sequence 4: GGAAGAUCUUGGACUUAUU.

Lipofectamine™ RNAiMAX Transfection Reagent (Thermo Fischer), Opti-MEM™ Reduced Serum Medium (Thermo Fischer) and 5x siRNA buffer (Dharmacon; Lafayette, CO, USA) was used. Knockdown effects were verified using qPCR or Western Blot analysis after 6 days.

Experimental readouts

Quantitative PCR analysis (qPCR) involved RNA isolation with TRIzolTM by manufacturer instructions (Invitrogen; Carlsbad, CA, USA). cDNA synthesis used Oligo(dT)20 Primer (Invitrogen), SuperScript IV Reverse Transcriptase (including buffer + DTT) (Invitrogen), dNTPs (Genecraft; Lüdinghausen, Germany) and Random Hexamers dN6 (Thermo Fischer). qPCR used Luminoct® SYBR Green qPCR Ready Mix (Sigma-Aldrich) and the following primer pairs (IDT; Coralville, Iowa, USA and Eurofins (Luxembourg):

ALDH1A1 Fw: GCACGCCAGACTTACCTGTC, Rv: CCTCCTCAGTTGCAGGATTAAAG; KDM1A Fw: TGACCGGATGACTTCTCAAGA, Rv: GTTGGAGAGTAGCCTCAAATGTC; KDM1B Fw: CTCTCCTGTGGGGAACATTTC, Rv: GACTAGGTTCGGTTTTGCCATT; KDM2B Fw: GGG TTCCCCTGATATTTCGAGA, Rv: GCTCCCCACTAGGAGTTTGAC; KDM5A Fw: GTCACCTGGAGCTAAGGCAC, Rv: CCGTTTCCGTTTC TTCTCTG; KDM5B Fw: AGTGGGGCTCACATATCAGAGG, Rv: CAAACACCTTAGGCTGTCTCC; KDM5C Fw: CTTGCTACGCTCCCACT ACG, Rv: TGTGTTACACTGCACAAGGTTG; KDM5D Fw: CAAGACCCGCTTGGCTACATT, Rv: TTGGACGCGAGGAGTAAATCT; KDM6A Fw: TACAGGCTCAGTTGTGTAACCT, Rv: CTGCGGGAATTGGTAGGCTC; RPL37A Fw: GACGTACAATACCACTTCCGC, Rv: GGAGC GTCTACTGGTCTTTCA.

A PCR Mastercycler nexus GX2 (Eppendorf, Hamburg, Germany) and a CFX96 Touch real-time cycler (BioRad, Hercules, CA, USA) were used. Relative gene expression was calculated by normalization to the housekeeper gene RPL37A.

Flow cytometry was conducted per standard methodology on a FACS Celesta (BD Biosciences; San Jose, CA, USA) using the FACS Diva software version v 8.0.1.1 (BD Biosciences). Data analysis was performed using FlowJo software, version v10.5.3. The gating strategy for detection of KDM5B^{high} cells, included the setting of a threshold on the 5% highest fluorescence intensity (TOP 5% EGFP-KDM5B reporter) as determined in the respective control sample (naive cells or DMSO). The control gate was projected onto each further sample to determine the frequency of experimental cells reaching the threshold.

The 7-AAD Viability Staining Solution (0.25µg/1x10^{6} cells; Thermo Fischer) was applied to single cell suspensions of indicated samples, derived from drug exposure studies, 5-10 minutes prior to flow cytometry analysis.

CellTrace™ Far Red solution (5µM in PBS; Thermo Fischer #C34572) was applied by manufacturer's instruction on indicated cell samples under adherent proliferative conditions, one hour before the indicated drug exposure. Proliferation analysis by flow cytometry was performed five days later.

Quantification of cellular phenotypes was performed on 0.25-0.5x10^{6} of the indicated patient cells in FACS buffer (2mM EDTA, 0.1 % BSA in 1x PBS) with human Fc Block (1:100; BD Biosciences, Franklin Lakes, NJ, USA, #564220, RRID: AB_2869554) for 15 min at RT. Cells were fixed and permeabilized by the BD Cytofix/Cytoperm™ Fixation/Permeabilization Kit (BD Biosciences) according to the manufacturer's protocol. Conjugated primary antibodies included: ALDH1A1 (FITC, 1:5, Abcam #ab275646, RRID: N/A) and pAKT (Ser473) (Alexa488, 1:2.5, BD Biosciences #560404, RRID: AB_1645342). The unconjugated KDM5B antibody (rabbit, 1:25, Novus #NB100-97821, RRID: AB_1291176) was combined with an Alexa-Fluor 555 coupled secondary antibody (goat anti-rabbit IgG, 1:200, Thermo Fisher Scientific #A21428, RRID: AB_2535849) or alternatively with an Alexa-Fluor 647 coupled secondary antibody (donkey anti-rabbit IgG, 1:400, BioLegend #406414; RRID:AB_2563202). Antibody solutions were incubated with cells for 30 min on ice. Prior to flow cytometry analysis, cells were washed and resuspended in FACS buffer.

The caspase assay was evaluated for active Caspase-3 accordingly, using appropriate antibodies (FITC, 1:5, BD Bioscience #559341, RRID: AB_397234) and methods prior to flow cytometry.

Cell confluence was determined in the cellular assays at indicated time points longitudinally using software-based cell recognition (Nyone®, Synentec, Elmshorn, Germany).

Cell viability was evaluated via alamarBlueTM assay (Life Technologies) following the manufacturer's instructions. Readout was performed on a Tecan Infinite F200 instrument (Tecan, Männedorf, Switzerland).

Protein expression analysis involved scrapping of cells using a lysis buffer (Pierce™ RIPA Buffer (Life Technologies) containing cOmplete™ Protease Inhibitor Cocktail (Roche; Basel, Switzerland) and PhosSTOP™ (Sigma-Aldrich). Protein concentration was measured using Thermo Scientific Pierce BCA Protein Assay (Thermo Fischer) and a Tecan Infinite F200 instrument. Total protein was separated by SDS-PAGE (4–15% Mini-PROTEAN® TGX™ Precast Protein Gels; BioRad) and transferred onto nitrocellulose membranes (Trans-Blot® Turbo™ Mini Nitrocellulose Transfer Packs; Biorad) by electroblotting. Membranes were blocked in 5% milk powder (Carl Roth GmbH, Karlsruhe, Germany) in PBS (Thermo Fischer) with 0.5% TWEEN®-20 (Sigma-Aldrich) (PBST) or alternatively in TBS (TRIS-Hydrochlorid (Carl Roth); Sodium chloride (Carl

Roth)) with 0.5% TWEEN®-20 (Sigma-Aldrich) (TBST) for 1 hour. The membranes were supplied with primary antibodies (KDM5B (1:250, Sigma-Aldrich #HPA027179, RRID: AB_1851987); PTEN XP® (1:1000, Cell signaling #9188P, RRID: AB_2253290); phospho-AKT (Ser473) XP® (1:2000, Cell signaling #4060S, RRID: AB_2315049); phospho-GSK3ß (Ser9) (1:1000, Cell signaling #5558P, RRID: AB_10013750); phospho-mTOR (Ser2448) XP® (1:1000, Cell signaling #5536P, RRID: AB_10691552); Cyclin D3 (1:1000, Cell signaling #2936, RRID: AB_2070801)) in 5% milk powder in PBST overnight at 4°C or for 1 hour at room temperature (β-actin (1:5000, Sigma-Aldrich #A5441, RRID: AB_476744). The primary antibodies PI3 Kinase p85 1:1000, Cell signaling #4292, RRID: AB_329869) and PI3 Kinase p110α (1:1000, Cell signaling #4255, RRID: AB_659888) were supplied in 5% BSA (Carl Roth) in TBST overnight at 4°C. The membranes were detected with horseradish peroxidase (HRP)-coupled secondary antibodies (anti-rabbit IgG, HRP-linked (1:2000, Cell signaling #7074, RRID: AB_2099233); Anti-mouse IgG, HRP-linked (1:2000, Cell signaling #7076, RRID: AB_330924)) using Clarity™ Western ECL Substrate (Biorad) and the ChemiDoc System (Biorad). For stripping the membrane was incubated with suitable stripping buffer before blocking with 5% milk and staining with primary and secondary antibodies as described above. Intensity quantification and normalization to ß-actin was performed using Image Lab™ software version 6.0.1 (Biorad).

Barcoding of glioblastoma patient cells

Indicated patient cells were barcoded by lentiviral infection with the Clontracer System.[28] The ClonTracer library (Addgene #67267) consists of semi-random 30-bp-long DNA barcodes with 15 repeats of alternating weak (A/T) and strong (G/C) bases and flanked by a pair of primer binding sites for barcode amplification, cloned into the lentiviral vector backbone pRSI9-U6-(sh)-UbiC-TagRFP-2A-Puro (Cellecta; Mountain View, CA, USA), containing puromycin resistance cassette and RFP as a fluorescent marker.

Lentivirus was produced in HEK293T cells using the TransIT-TKO® transfection reagent Mirus (Mirus Bio; Madison, Wisconsin, USA), Opti-MEM™ Reduced Serum Medium (Thermo Fisher Scientific) and the following plasmids: 2.4μg ClonTracer Barcoding Library (containing barcodes, RFP and puromycin resistance cassette, Addgene #67267; RRID: Addgene_67267), 2.4μg pCMV delta R8.2 (Addgene #12263; RRID: Addgene_12263), 1.2μg pCMV-VSV-G (Addgene #8454; RRID: Addgene_8454). 10×10^6 cells were infected with an efficiency of 10 - 30% (RFP-based flow cytometry) to uniquely barcode each of the 10^6 cells.[26] Selection of barcoded cells was performed by puromycin (Thermo Fisher Scientific) and verified by flow cytometry through RFP.

For NGS analysis, DNA was isolated from harvested samples using the Gentra Puregene Precipitation Kit (Qiagen; Hilden, Germany) as instructed by the manufacturer. A PCR was performed to enrich the barcode region using KAPA HiFi HotStart ReadyMix (Roche): with the forward primer (all Eurofins; Luxembourg):

(5′-3′) AATGATACGGCGACCACCGAGATCTACACACTGACTGCAGTCTGAGTCTGACAG and 12 different reverse Index primers (for multiplex sequencing):

(5′-3′) CAAGCAGAAGACGGCATACGAGAT - (index of 6 bases) -GTGACTGGAGTTCAGACGTGTGCTCTTCCGATCTCTAGCATAG AGTGCGTAGCTCTGCT.

Pooled, PCR-amplified and gel-purified (QIAquick Gel Extraction Kit; Qiagen; Hilden, Germany) products were sent for sequencing on an Illumina HiSeq 2000 v4 single-read 50bp platform or a NextSeq 550 single-read 75bp using the Multiplex Index Type Illumina TruSeq. For sequencing the following primer was used: (5′-3′) ACACACTGACTGCAGTCTGAGTCTGACA (Eurofins). Additionally, Illumina primers were used for sequencing PhiX v3 and the index sequence of pooled samples. The Illumina bcl2fastq 2.20.0.422 Conversion Software was used to demultiplex sequencing data and convert base call (BCL) files into FASTQ files. Quality control of the sequencing data was performed using the FastQC Reports. The barcode representation for each sample (reads per barcode per sample) was extracted from the FASTQ files from the barcode-sequencing runs, using a custom-written Python script (version 3.9.9) according to the Clontracer System.[28] Only the 30N barcodes, which consisted of alternating weak and strong base pairs and were bordered by specific flanking sequences, were further analyzed. Barcode reads were normalized by dividing reads per barcode by total read count of the sample. Bubble plots showing relative abundance were generated in R (version 4.1.2) by using the ggplot2 package (version 3.3.6), showing only barcodes above or equal to a threshold of 1%, in at least one of the samples. Stacked plots were generated using R (software version 4.2.2) for the TOP50 DTEP barcodes in each sample, stacked to 100%.

QUANTIFICATION AND STATISTICAL ANALYSIS

Unless otherwise specified, data are presented as mean ± SD. Statistical methods, including corrections for multiple testing are described in each set of data. The significance threshold was set at 0.05. R (The R Foundation for Statistical Computing, v4.1.3) and GraphPad Prism v8 were used for statistical analysis. Statistical details of the experiments can be found in the figure legends.